Eur. Phys. J. A **30**, 443–453 (2006)
DOI 10.1140/epja/i2006-10133-6

THE EUROPEAN PHYSICAL JOURNAL A

Single-pion production in pp collisions at 0.95 GeV/c (I)

The COSY-TOF Collaboration

S. Abd El-Samad[8], R. Bilger[6], K.-Th. Brinkmann[2], H. Clement[6,a], M. Dietrich[6], E. Doroshkevich[6], S. Dshemuchadse[5,2], A. Erhardt[6], W. Eyrich[3], A. Filippi[7], H. Freiesleben[2], M. Fritsch[3,1], R. Geyer[4], A. Gillitzer[4], J. Hauffe[3], D. Hesselbarth[4], R. Jaekel[2], B. Jakob[2], L. Karsch[2], K. Kilian[4], H. Koch[1], J. Kress[6], E. Kuhlmann[2], S. Marcello[7], S. Marwinski[4], R. Meier[6], K. Möller[5], H.P. Morsch[4], L. Naumann[5], E. Roderburg[4], P. Schönmeier[2,3], M. Schulte-Wissermann[2], W. Schroeder[3], M. Steinke[1], F. Stinzing[3], G.Y. Sun[2], J. Wächter[3], G.J. Wagner[6], M. Wagner[3], U. Weidlich[6], A. Wilms[1], S. Wirth[3], G. Zhang[6,b], and P. Zupranski[9]

[1] Ruhr-Universität Bochum, Germany
[2] Technische Universität Dresden, Germany
[3] Friedrich-Alexander-Universität Erlangen-Nürnberg, Germany
[4] Forschungszentrum Jülich, Germany
[5] Forschungszentrum Rossendorf, Germany
[6] Physikalisches Institut der Universität Tübingen, Auf der Morgenstelle 14, D-72076 Tübingen, Germany
[7] University of Torino and INFN, Sezione di Torino, Italy
[8] Atomic Energy Authority NRC Cairo, Egypt
[9] Soltan Institute for Nuclear Studies, Warsaw, Poland

Received: 10 July 2006 / Revised: 16 October 2006 /
Published online: 13 November 2006 –
Communicated by M. Garçon

Abstract. The single-pion production reactions $pp \to d\pi^+$, $pp \to np\pi^+$ and $pp \to pp\pi^0$ were measured at a beam momentum of 0.95 GeV/c ($T_p \approx 400$ MeV) using the short version of the COSY-TOF spectrometer. The implementation of a central calorimeter provided particle identification, energy determination and neutron detection in addition to time-of-flight and angle measurements. Thus, all pion production channels were recorded with 1–4 overconstraints. The total and differential cross-sections obtained are compared to previous data and theoretical calculations. Main emphasis is put on the discussion of the $pp\pi^0$ channel, where we obtain angular distributions different from previous experimental results, however, partly in good agreement with recent phenomenological and theoretical predictions. In particular, we observe very large anisotropies for the π^0 angular distributions in the kinematical region of small relative proton momenta revealing there a dominance of proton spinflip transitions associated with π^0 s and d partial waves and emphasizing the important role of π^0 d-waves.

PACS. 13.75.Cs Nucleon-nucleon interactions (including antinucleons, deuterons, etc.) – 25.10.+s Nuclear reactions involving few-nucleon systems – 25.40.Ep Inelastic proton scattering – 29.20.Dh Storage rings

1 Introduction

Single-pion production in the collision between two nucleons is thought to be the simplest inelastic process between two baryons. Therefore, it came as a surprise, when first near-threshold data on the $pp\pi^0$ channel [1] revealed its cross-section to be larger than predicted [2–4] by nearly one order of magnitude. Meanwhile, the near-threshold data base has been much improved by exclusive measurements at TRIUMF (TINA and MINA) [5], SATURNE (SPES0) [6] and in particular at the cooler storage rings CELSIUS (PROMICE/WASA) [7–9], COSY (GEM, TOF) [10,11] and IUCF [12], at the latter also with polarized beam and target. However, this data base is still far from being complete and often simple, but very useful observables like angular and invariant-mass distributions or even Dalitz plots of the unpolarized cross-section are still missing. Moreover, the partial-wave analyses of IUCF and PROMICE/WASA data lead to different conclusions. In order to contribute to a clarification of the situation we report in this paper on the first kinematically complete high-statistics measurement of differential cross-sections at a beam momentum of 0.95 GeV/c (corresponding to $T_p = 397$ MeV) for the reactions $pp \to d\pi^+$, $pp \to pp\pi^0$

[a] e-mail: clement@pit.physik.uni-tuebingen.de
[b] *Present address:* Peking University, PRC.

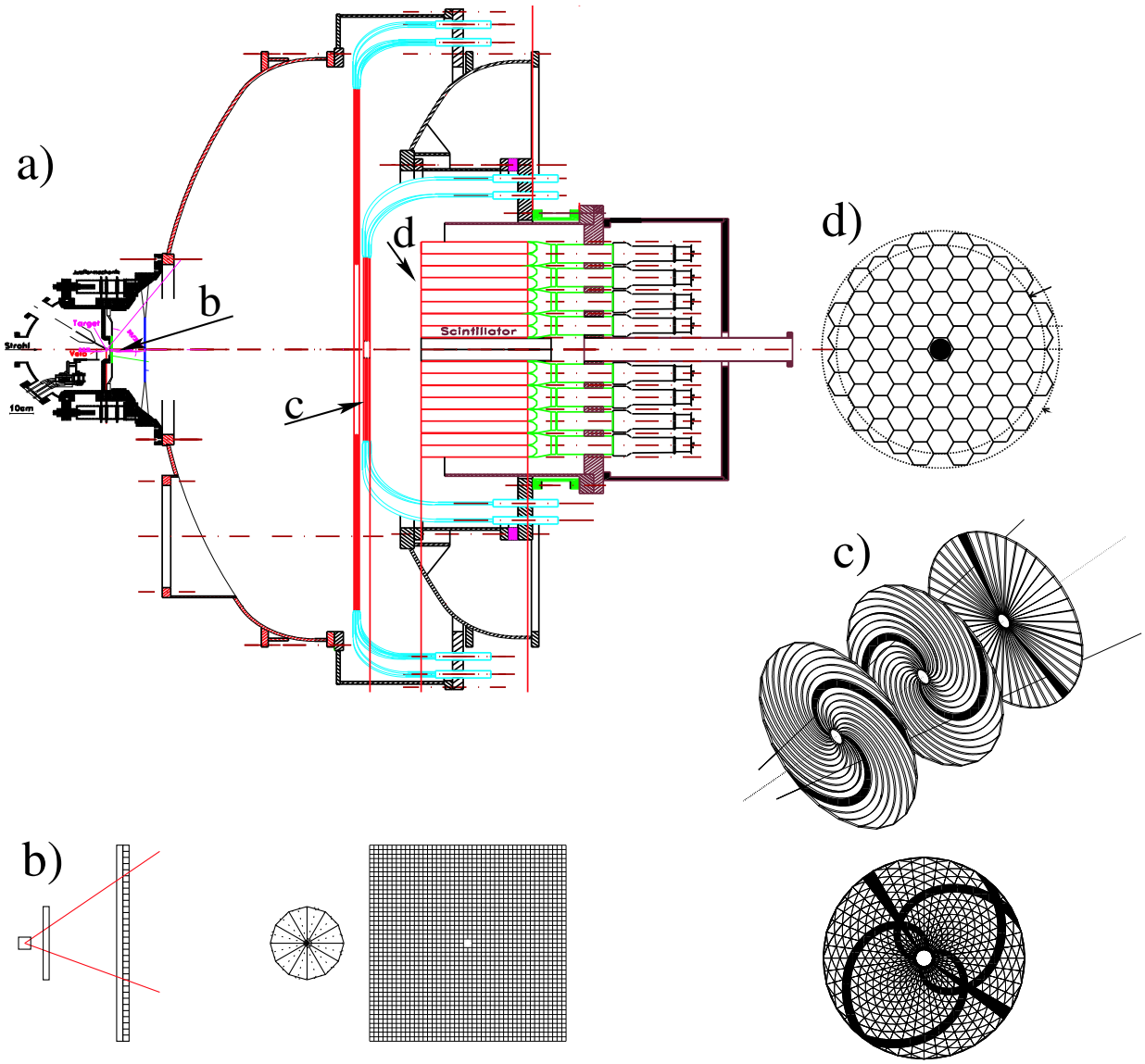

Fig. 1. Sketch of the short COSY-TOF setup used in this experiment showing a) the full detector arrangement with inserts for b) the start detector region with start wedges and hodoscope displaying both side (left) and front (right) views, c) the central hodoscope ("Quirl") as the stop detector for TOF measurements and d) the central calorimeter. The positions of the subdetector systems (b–d) in the full setup are indicated in a). For a detailed description see text.

and $pp \to np\pi^+$. For the latter we give here the total cross-section only, the differential distributions will be discussed in a separate paper.

2 Experiment

The measurements have been carried out at the Jülich Cooler Synchrotron COSY using the time-of-flight spectrometer TOF at one of its external beam lines, where the accuracy of the beam momentum is known to be better than 1%. The setup of the TOF detector system is displayed in fig. 1. At the entrance of the detector system the beam —collimated to a diameter smaller than 2 mm— hits the LH_2 target, which has a length of 4 mm, a diameter of 6 mm and 0.9 μm thick hostaphan foils as entrance and exit windows [13]. At a distance of 22 mm downstream of the target the two layers of the start detector (each consisting of 1 mm thick scintillators cut into 12 wedge-shaped sectors) were placed followed by a two-plane fiber hodoscope (96×96 fibers, 2 mm thick each) at a distance of 165 mm from target, see fig. 1b. Whereas the start detector mainly supplies the start times for the time-of-flight (TOF) measurements, the fibre hodoscope primarily pro-

vides a good angular resolution for the detected particle tracks. In its central part the TOF-stop detector system consists of the so-called Quirl, a 3-layer scintillator system 1081 mm downstream of the target shown in fig. 1c and described in detail in ref. [14] —and in its peripheral part of the so-called Ring, also a 3-layer scintillator system built in a design analogous to the Quirl, however, with inner and outer radii of 560 and 1540 mm, respectively. Finally, behind the Quirl a calorimeter (figs. 1a,d) was installed for identification of charged particles and of neutrons as well as for measuring the energy of charged particles. The calorimeter, details of which are given in ref. [15], consists of 84 hexagon-shaped scintillator blocks of length 450 mm, which suffices to stop deuterons, protons and pions of energies up to 400, 300 and 160 MeV, respectively. The energy calibration of the calorimeter was performed by the detection of cosmic muons. In the experiment the trigger was set to two hits in Quirl and/or Ring associated with two hits in the start detector. From straight-line fits to the hit detector elements tracks of charged particles are reconstructed. They are accepted as good tracks, if they originate in the target and have a hit in each detector element the track passes through. In this way the angular resolution is better than 1° both in azimuthal and in polar angles. If there is an isolated hit in the calorimeter with no associated hits in the preceding detector elements, then this hit qualifies as a neutron candidate (further criteria will be discussed below). In this case the angular resolution of the neutron track is given by the size of the hit calorimeter block, *i.e.* by 7–8°. By construction of the calorimeter a particle will hit one or more calorimeter blocks. The number of blocks hit by a particular particle is given by the track reconstruction. The total energy deposited by this particle in the calorimeter is then just the (calibrated) sum of energies deposited in all blocks belonging to the particular track.

In order to have maximum angular coverage by the detector elements and to minimize the fraction of charged pions decaying in flight before reaching the stop detectors, the short version of the TOF spectrometer was used. In this way a total polar angle coverage of $3° \leq \Theta^{lab} \leq 49°$ was achieved with the central calorimeter covering the region $3° \leq \Theta^{lab} \leq 28°$. For fast particles the 4% energy resolution of the calorimeter is superior to that from TOF measurements, the resolution of which is reduced by the short path length. However, the TOF resolution is still much better than the ΔE resolution of the Quirl elements. Hence, for particle identification, instead of plotting ΔE *versus* E_{cal}, the uncorrected particle energy deposited in the calorimeter, we utilize the relation $\Delta E \sim (z/\beta)^2$ with the particle charge $z = 1$ and plot $1/\beta^2$ *versus* E_{cal}, where the particle velocity $\beta = v/c$ is derived from the TOF measurement.

Figure 2 shows at the top the $1/\beta^2$-E_{cal} scatterplot for two-track events. The bands for d, p and π are well separated. The horizontal shadow region on the left of the deuteron band stems from deuteron breakup in the calorimeter. Note that E_{cal} in fig. 2 is not yet corrected for energy- and particle-dependent quenching effects. By

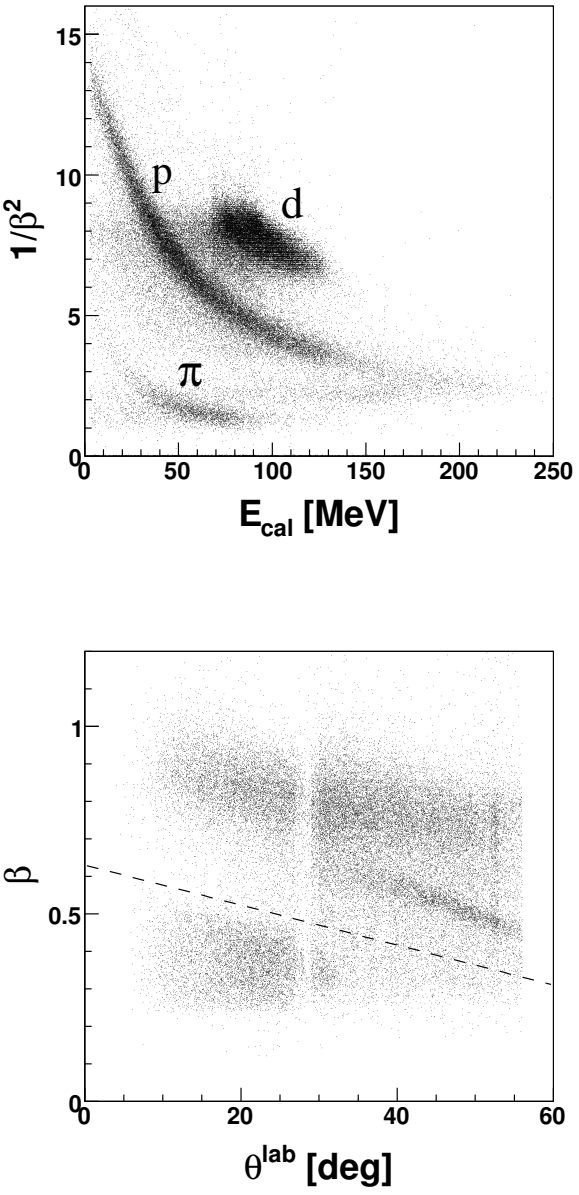

Fig. 2. Top: ΔE-E plot for particles stopped in the calorimeter. Shown is the first (smaller angle) track of two-track events. For the plot the ΔE information is taken from the TOF information obtained by Quirl and start detectors and plotted as $1/\beta^2$, where $\beta = v/c$ denotes the particle velocity normalized to c. For the E information the energy deposited in the calorimeter E_{cal} has been taken. Bottom: scatterplot for particles detected at the lab polar angle Θ^{lab} with velocity β stemming from two-track events, where the first track has been identified in the calorimeter as a proton. The dashed line separates the low-β region from the high-β region. The latter contains a broad band due to pions from the $np\pi^+$ channel and a narrow band from remnants of elastic scattering. The low-β region contains the proton band from the $pp\pi^0$ channel for $\Theta^{lab} < 33°$ and unidentified background. The vertical low-statistics band stems from the not perfect overlap in the angular regions covered by Quirl ($\Theta^{lab} < 28°$) and Ring, respectively.

applying the quenching correction as well as the correction for energy loss in the preceding detector elements the kinetic energies of the detected particles are deduced. At the bottom of fig. 2 the β-Θ^{lab} scatterplot is shown for particles detected at the lab polar angle Θ^{lab} with velocity $\beta = v/c$ and stemming from two-track events, where the first track has been identified in the calorimeter as a proton. The dashed line separates the low-β region from the high-β region. Whereas the latter contains a broad band due to pions from the $np\pi^+$ channel and a narrow band from remnants of elastic scattering, the low-β region contains only the proton band from the $pp\pi^0$ channel for $\Theta^{lab} < 33°$ and unidentified background.

By identifying and reconstructing the two charged tracks of an event the exit channels $d\pi^+$, $np\pi^+$ and $pp\pi^0$ can be separated. Kinematically the maximum possible laboratory (lab) polar angles are $\approx 9°$ for deuterons and $\approx 32°$ for protons (and neutrons). Hence 88% of the angular coverage for deuterons and 86% of that for protons from single pion production are within the angular acceptance of the calorimeter. For charged pions the angular coverage has been much lower with this setup, since kinematically they can extend up to $\Theta^{lab} = 180°$. Hence within the angular coverage of Quirl and Ring the angular acceptance for π^+ has been $\approx 40\%$ only. Nevertheless most of the phase space part necessary for a full coverage of the physics in single pion production has been covered (see below) by these measurements due to the circumstance that the center-of-mass (cm) angular distributions have to be symmetric about 90° because of identical collision partners in the incident channel.

For $\Theta^{lab} \leq 25.5°$ the $pp\pi^0$ events have been identified by requiring the two charged tracks of the events to be protons identified in the Quirl-calorimeter system. For $\Theta^{lab} > 28°$ the protons of the $pp\pi^0$ channel have been detected in the Ring. Since kinematically they have a small β they are easily distinguished from pions hitting the Ring and also from elastically scattered protons as demonstrated in fig. 2, bottom. The same applies for the angular region $25.5° < \Theta^{lab} \leq 28°$, where the protons hit only the edge of the calorimeter and in general no longer stop there. In both cases the proton energy is calculated from the corresponding TOF measured by the Start-Ring and Start-Quirl detector systems, respectively. Thus the full kinematically accessible angular range was covered for this reaction channel with exception of the beam-hole region ($\Theta^{lab} \leq 3°$). As further condition we required that the missing mass MM_{pp} reconstructed from the four-momentum vectors of two identified protons is in accordance with the mass of the π^0 not detected in this measurement. The missing mass spectrum is shown in fig. 3 for all events identified as $pp\pi^0$ candidates. In essence it is free from background. The small low-mass tail stems solely from events, where the second track has been detected in the Ring. It could have been reduced substantially by a much tighter cut around the region kinematically allowed for protons originating from single pion production events (see fig. 2, bottom). However, such events are anyway removed by the subsequent kinematic fit. This is also the reason why we needed to apply only a very loose cut on the missing mass MM_{pp} by the constraints $100\,\mathrm{MeV}/c^2 \leq MM_{pp} \leq 180\,\mathrm{MeV}/c^2$.

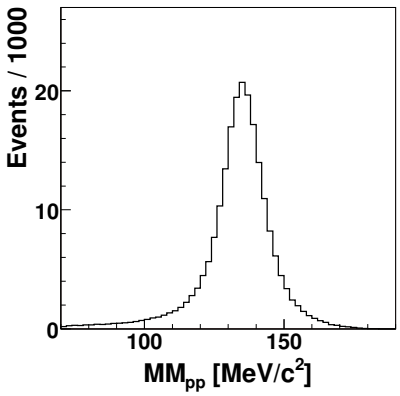

Fig. 3. Spectrum of the missing mass MM_{pp} reconstructed from the detected proton pairs for the $pp\pi^0$ channel.

The $d\pi^+$ events have been selected by identifying both deuteron and pion, if both hit the calorimeter or by identifying only the deuteron, if the pion hits the Ring. Corresponding missing-mass checks have been applied. In addition, the coplanarity condition $170° < \Delta\Phi \leq 180°$[1] was used to further distinguish $d\pi^+$ events from the three-body background. That way even the deuteron identification in the calorimeter may be omitted, thus allowing to check how well the deuteron breakup in the calorimeter is under control in the Monte Carlo (MC) simulations. Within uncertainties both ways lead to identical results.

Finally, the $np\pi^+$ channel was selected by identifying proton and pion in the calorimeter or only the proton in the calorimeter, when the second charged track is in the Ring. In addition the missing $p\pi$ mass $MM_{p\pi}$ has to meet the condition $900\,\mathrm{MeV}/c^2 \leq MM_{p\pi} \leq 980\,\mathrm{MeV}/c^2$. Also to suppress background from the $d\pi^+$ channel —in particular when the deuteron is broken up and appears as a proton in the calorimeter— the $p\pi^+$ track is required to be non-coplanar, *i.e.* $\Delta\Phi < 170°$ complementary to the coplanarity condition given above. Further on the neutron 4-momentum is reconstructed from the 4-momenta of proton and pion and it is checked, whether a calorimeter block in the corresponding (Θ, Φ) region recorded a hit accompanied without any entries recorded in the preceding detector elements of the Quirl. If these conditions are met, a neutron track is assumed. That way Θ_n and Φ_n are determined by the location of this calorimeter block. Thus, having only the neutron energy undetermined experimentally we end up with 3 kinematic overconstraints for this channel, whereas we have 1 overconstraint for the $pp\pi^0$ channel and 4 overconstraints for the $d\pi^+$ channel. Corresponding kinematic fits were applied and only events were considered in further analyses, where the χ^2 converged with $\mathrm{prob}(\chi^2) > 5\%$.

[1] $\Delta\Phi$ is defined as the projection of the opening angle between two tracks onto the plane normal to the beam vector. That way we have always $\Delta\Phi \leq 180°$.

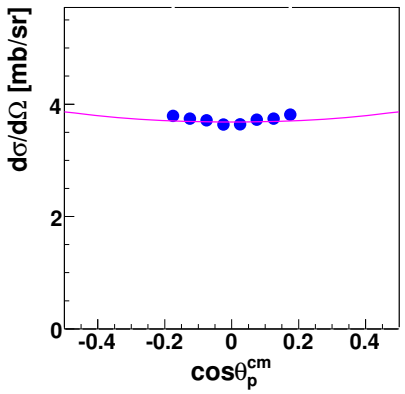

Fig. 4. Angular distribution of *pp* elastic scattering in the cm system. The data of elastic-scattering proton pairs recorded in the Ring detector (full circles) have been adjusted in absolute height to the SAID [16] data base (solid line).

The luminosity of the experiment was determined from the analysis of *pp* elastic scattering. Due to their opening angle of $\delta_{pp} \approx 84°$ between both tracks, such two-track events have both hits in the Ring. They are easily identified by using in addition the coplanarity constraint $170° < \Delta\Phi \leq 180°$. Figure 4 shows the measured angular distribution in comparison with the prediction from the SAID database [16]. The histogram of fig. 4 has been filled using both tracks of the elastic events. This way we have plotted in fig. 4 not only the data for $\Theta^{cm} \leq 90°$, which would be sufficient from the physics point of view, but also the region $\Theta^{cm} \geq 90°$, which serves as a check for systematic errors as discussed at the beginning of the next section. All data have been efficiency corrected by MC simulations of the detector setup by using the CERN GEANT3 [17] detector simulation package, which accounts both for electromagnetic and hadronic interactions of the ejectiles with the detector materials. Whereas the efficiency for the reconstruction of the simple elastic events is 0.96, the efficiency for the reconstruction of the much more complicated $pp\pi^0$ events is 0.67, since there the protons stopping in the calorimeter undergo substantial hadronic interaction with the scintillator material on their passage through the calorimeter blocks. Adjustment of the *pp* elastic data in absolute height to the SAID values gives the required luminosity ($L = 5 * 10^{33}\,\mathrm{cm}^{-2}$ and $\mathrm{d}L/\mathrm{d}t = 3 * 10^{28}\,\mathrm{cm}^{-2}\,\mathrm{s}^{-1}$ time averaged). The one-parameter χ^2 fit on the data gives a value of 4.3 per degrees of freedom, which means that the data sample contains systematic uncertainties in the order of twice the statistical ones. Sources of systematic errors include track reconstruction, kinematic fit and imperfections in rebuilding the real TOF detector in the GEANT detector simulation package. By visual inspection of the data plotted in fig. 4 we arrive at the conclusion that a conservative estimate of an upper bound for the systematic uncertainties is given by the size of the symbols used in fig. 4, *i.e.* in the order of 4%. Note that since all data presented in this paper have been obtained by use of the same trigger and with same DAQ system, their efficiencies drop out in the normalization of the single pion production data relative to the elastic ones.

Table 1. Total cross-sections σ_{tot} at $T_p \approx 400\,\mathrm{MeV}$ for the reactions $pp \to d\pi^+$, $pp \to np\pi^+$ and $pp \to pp\pi^0$ evaluated in this work and compared to previous measurements.

σ_{tot} [mb]		
$pp \to d\pi^+$	$pp \to np\pi^+$	$pp \to pp\pi^0$
0.74 (2)	0.47 (2)	0.100 (7)
0.72[a)]		0.092 (7)[b)]
		0.070 (7)[c)]

[a)] Reference [16].
[b)] Reference [9].
[c)] Reference [5].

3 Results

Due to the identity of the collision partners in the entrance channel the angular distributions in the overall center-of-mass system have to be symmetric about 90°, *i.e.* the full information about the reaction channels is contained already in the interval $0° \leq \Theta^{cm} \leq 90°$. Deviations from this symmetry in the data indicate systematic uncertainties in the measurements. Hence we plot —where appropriate— the full angular range, in order to show the absence of major systematic errors present in our measurement. With the exception of fig. 11 the statistical errors are smaller than the symbols used for the presentation of the data points.

The evaluated total cross-sections for the three channels are given in table 1 together with previous results. The uncertainties assigned are based on systematics for acceptance and efficiency corrections as obtained by variation of MC simulations for the detector response, where we have varied the MC input assuming either pure phase space or some reasonable models for the reaction under consideration. Statistical uncertainties are negligible compared to the systematic uncertainties.

3.1 pp → dπ$^+$

Absolute and differential cross-sections for this reaction channel are very well known from previous experiments. Hence we use the analysis of our data for this channel primarily as a check of the reliability of our measurement and data analysis. In fig. 5 our results for the π^+ angular distribution are shown in comparison with the prediction from the SAID data base [16]. Since in the measurement we cover only angles $\Theta_\pi^{cm} < 90°$ we show in fig. 5 only the appropriate half of the full angular distribution. Note, however, that due to the symmetry of the angular distribution around $\cos\Theta_\pi^{cm} = 0$ most of the physically relevant phase space part has been covered in this measurement. We find good agreement with the SAID data base both

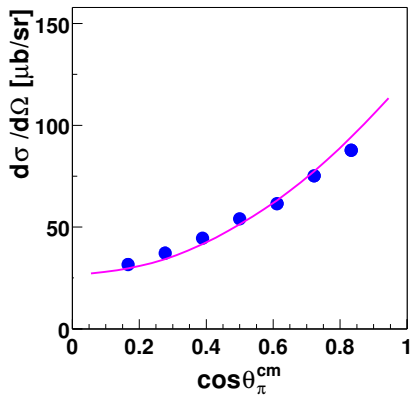

Fig. 5. Pion angular distribution in the cm system for the reaction $pp \to d\pi^+$. The data of this work (full circles) are compared to the SAID [16] data base (solid line).

in absolute magnitude and in the shape of the angular distribution. Since the pions of this channel cover the angular range of both Quirl and Ring, *i.e.*, stem from Quirl-Quirl and Quirl-Ring coincidences, the good agreement with SAID assures that there are no significant problems with correlating the efficiencies of Quirl and Ring.

3.2 pp → ppπ^0

This channel has received increasing attention since first measurements in the threshold region [12] at IUCF and later also at CELSIUS [7] uncovered the total cross-section to be nearly an order of magnitude larger than predicted theoretically [2–4]. Very recent close-to-threshold measurements at COSY-TOF revealed the experimental total cross-sections to be even larger by roughly 50% [11] than previously measured. There it was shown that the pp final-state interaction (FSI) has a very strong influence on the reaction dynamics close to threshold with the consequence that a substantial part of the cross-section is at small lab angles, which were missed in IUCF and CELSIUS measurements near threshold. At higher energies, 320 MeV $\leq T_p \leq$ 400 MeV, where the influence of the pp FSI decreases more and more, the total cross-section data measured at TRIUMF [5], SATURNE [6], COSY-GEM [10] and CELSIUS (PROMICE/WASA) [9] are in agreement with each other with the exception of a 20% discrepancy at $T_p \approx 400$ MeV between CELSIUS and TRIUMF results. Our value, see table 1, is in agreement with the CELSIUS result. Recent measurements with polarized beam [6] and partly also polarized target [1] added much to the detailed knowledge of this reaction from threshold up to $T_p \approx 400$ MeV.

Despite the wealth of experimental information on this reaction there remain a number of problems, which are not yet sufficiently settled. *E.g.* the anisotropy of the pion angular distribution in the overall cm system, characterized by the anisotropy parameter b, which traditionally [5,6] is defined by

$$\sigma(\Theta_{\pi^0}^{cm}) \sim 1/3 + b * \cos^2 \Theta_{\pi^0}^{cm}, \qquad (1)$$

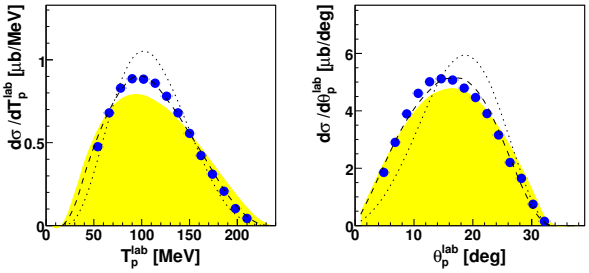

Fig. 6. Spectra for kinetic energies and polar angles (lab system) of detected proton pairs stemming from the $pp \to pp\pi^0$ reaction. The shaded areas show the corresponding phase space distributions for comparison. Dashed and dotted lines give calculations with the ansatz eq. (4) and the ansatz of ref. [8], *i.e.* eq. (3), respectively.

where $\Theta_{\pi^0}^{cm}$ denotes the π^0 polar angle in the overall cm system, shows a big scatter in the results from different measurements, see, *e.g.*, fig. 11 in ref. [11] for $T_p \leq 400$ MeV and fig. 6 in ref. [6] for higher incident energies. Note that in ref. [11] the Legendre coefficient a_2 for p-waves is plotted according to the ansatz

$$\sigma(\Theta_{\pi^0}^{cm}) \sim 1 + a_2 * (3\cos^2 \Theta_{\pi^0}^{cm} - 1)/2. \qquad (2)$$

In this paper we will use eq. (2) analogously also for fitting the experimental proton angular distributions $\sigma(\Theta_p^{pp})$ by replacing $\Theta_{\pi^0}^{cm}$ with Θ_p^{pp}, the proton angle in the pp subsystem. The parameters b and a_2 are related by $a_2 = 2b/(1+b) \approx 2b$ for $b \ll 1$. We will use the quantity a_2 in the following discussion of the angular distributions.

Near-isotropy is found for $T_p < 400$ MeV with a_2 staggering between -0.1 and $+0.1$ —with a tendency to negative values. The latter would mean that d-wave contributions inducing negative a_2 values are already present close to threshold [8]. A clearer trend towards positive a_2 values is observed for $T_p > 400$ MeV.

As we will show below, our results for a_2 are at variance with previous results and hence need a more detailed consideration. To this end, we start the presentation and discussion of our results first with energy and angular distributions of the protons in the lab system as displayed in fig. 6. In this and in the following one-dimensional figures phase space distributions are shown by shaded areas for comparison. We see that the data do not deviate vigorously from the phase space distributions, as we would expect, *e.g.* if Δ excitation would play a dominant role in this reaction channel. This is also visible in the experimental Dalitz plots of $M^2_{p\pi^0}$ *versus* M^2_{pp} and $M^2_{p\pi^0}$ *versus* $M^2_{p\pi^0}$ displayed in fig. 7. The data cover essentially the full available elliptical phase space areas and yield distributions, which are close to flat with just one pronounced excursion in the region of the pp FSI. This is reflected also in the projections of the Dalitz plot leading to the spectra of the invariant masses $M_{p\pi^0}$ and M_{pp} (fig. 8). The latter exhibits a small spike at the pp threshold due to pp FSI, though in total its influence is of minor importance as expected from the small amount of s-wave between the two protons being available at this energy [12]. In the $M_{p\pi^0}$ spectrum we

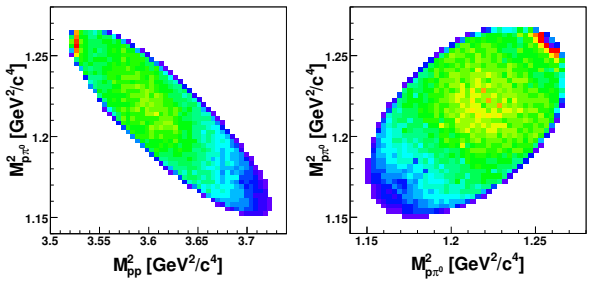

Fig. 7. Dalitz plots for the invariant-mass combinations $M^2_{p\pi^0}$ *versus* M^2_{pp} and $M^2_{p\pi^0}$ *versus* $M^2_{p\pi^0}$ as obtained from the data for the $pp \to pp\pi^0$ reaction. Note that the plots are efficiency but not acceptance corrected, hence the tiny deviations from the elliptic circumference at the upper corners due to the excluded beam-hole region.

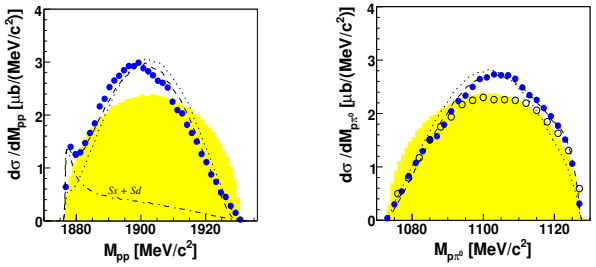

Fig. 8. Differential cross-sections in dependence on invariant masses M_{pp} and $M_{p\pi^0}$ for the $pp \to pp\pi^0$ reaction. Data of this work are shown by full circles, the ones from ref. [9] by open circles and phase space by the shaded area. For the explanation of dashed and dotted lines see caption of fig. 6. The dash-dotted lines in the M_{pp} distribution show the partial-wave contributions $Ss + Sd$ as obtained from eq. (4).

compare our data with the ones from CELSIUS as given in ref. [9]. We find agreement between both data sets with the exception of the region around $M_{p\pi^0} \approx 1100\,\mathrm{MeV}/c^2$, where we obtain a somewhat larger yield.

Now we turn again to the angular distributions, which are shown in fig. 9, on the top left for the pions denoted by their cm polar angles $\Theta^{cm}_{\pi^0}$ and on the top right for protons in the *pp* subsystem (Jackson frame) denoted by Θ^{pp}_{p}, *i.e.* we use the same coordinate system scheme as defined in the IUCF publication [12]. In addition, we plot at the bottom of fig. 9 also the proton angular distribution in the overall cms, in order to enable comparison with the corresponding results from ref. [9]. All distributions are close to flat, exhibit, however, a clearly negative anisotropy parameter with $a_2 = -0.12(1)$ for pions and $a_2 = -0.10(1)$ for protons.

4 Discussion of results

The negative anisotropy parameter observed in this experiment for the π^0 angular distribution comes as a surprise, since all previous experiments around $T_p \approx 400\,\mathrm{MeV}$ gave —or indicated at least— a positive value

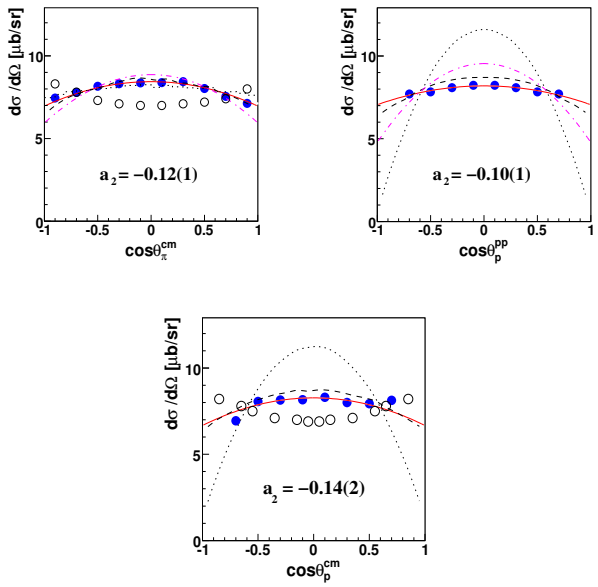

Fig. 9. Angular distributions of pions (overall cm system) and protons (*pp* subsystem, Jackson frame —as well as overall cm system at the bottom) for the $pp \to pp\pi^0$ reaction. Data of this work are shown by full circles, the fit to the data with eq. (2) by solid lines, the results of ref. [9] by open circles and the prediction of ref. [22] by the dash-dotted curve. For the explanation of dashed and dotted lines, see caption of fig. 6.

for the pions, the most serious discrepancy being with the PROMICE/WASA results [9] of $a_2 = +0.127(7)$ (note that the b values given in [9] need to be divided by a factor of 3, in order to comply with our definition of b in eq. (1)), since that measurement provided the best statistics and phase space coverage of all previous experiments at this energy. Although ref. [9] reports negative a_2 values for $T_p \leq 360\,\mathrm{MeV}$, positive values are found for $T_p \geq 400\,\mathrm{MeV}$.

From their analysis of polarization data the authors of ref. [12] also find some predictions for the unpolarized angular distributions, though with very large uncertainties. For protons they get $a_2 = -0.34(81)$ and for pions $a_2 = 0.17(11)$. The first one agrees in sign and value with our results, however, their value for the pions has an opposite sign. Nevertheless, since these numbers were obtained only indirectly with very large uncertainties, this is not a point of major concern —in particular since π^0 d-waves, which as we demonstrate in this paper are vital for a proper understanding of the reaction, are not taken into account in ref. [12]. We also note that a recent measurement of this reaction at $T_p = 400\,\mathrm{MeV}$ was carried out at CELSIUS-WASA, too. The results of this analysis also provide a negative a_2 parameter for the pion angular distribution [18,19]. If we restrict our data to the same proton angular range as covered in the CELSIUS-WASA experiment, then we find full consistency between both results.

On the theoretical side extensive meson-exchange calculations as well as partial-wave analyses were carried out very recently by the Jülich theory group [20–22]. Their

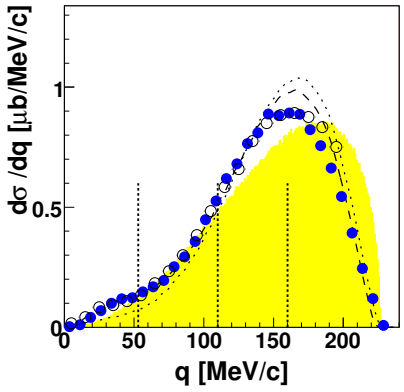

Fig. 10. Differential cross-section in dependence of q, which is half of the relative momentum between the proton pair ($q^2 = M_{pp}^2/4 - m_p^2$). Data of this work (full circles) are compared to results from ref. [9] (open circles) and to phase space (shaded area). For ease of comparison the data from ref. [9] have been normalized to the maximum of our distribution. For the explanation of dashed and dotted lines, see caption of fig. 6.

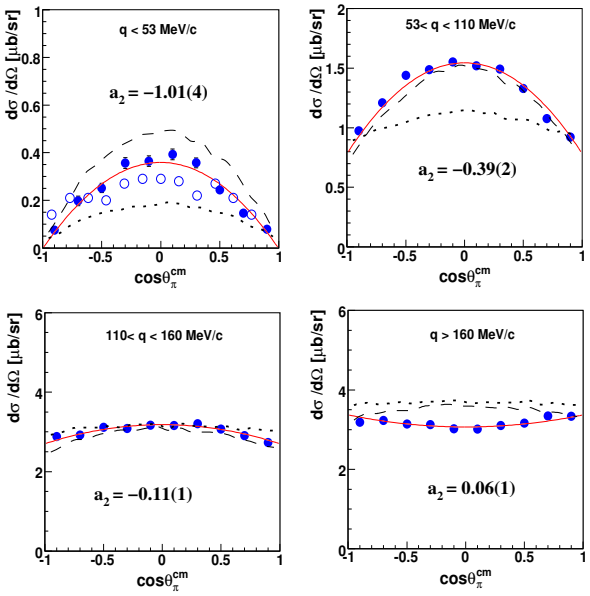

Fig. 11. Pion angular distributions (overall cm system) for 4 different q ranges as indicated for the $pp \to pp\pi^0$ reaction. Data from this work are shown by full circles, the fit to the data with eq. (2) by solid lines. For the explanation of dashed and dotted lines, see caption of fig. 6. The open circles show the results of ref. [9] as given in ref. [19], *i.e.*, not averaged over Θ_π^{cm} and $180^\circ - \Theta_\pi^{cm}$.

calculations are partly in good agreement with the polarization data. Interestingly, their prediction for proton and pion angular distributions (shown in fig. 9 by the dash-dotted lines) also results in negative a_2 values in agreement with our results. More advanced calculations based on chiral perturbation theory are in progress. First steps in this direction have already been taken by this group [23].

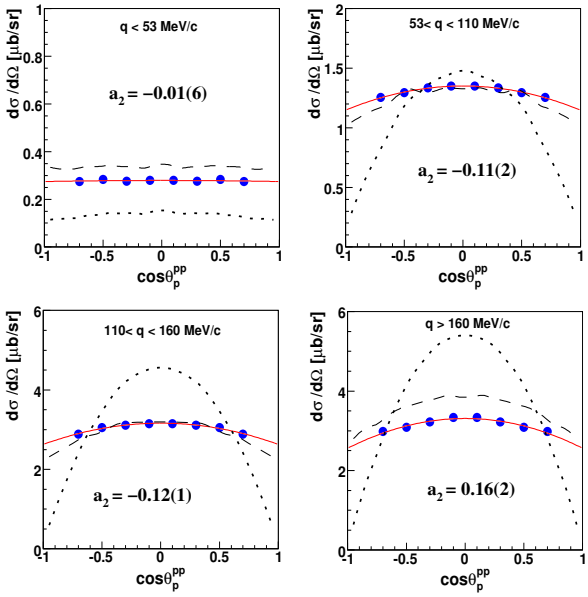

Fig. 12. Proton angular distributions (pp subsystem, Jackson frame) for 4 different q ranges as indicated for the $pp \to pp\pi^0$ reaction. Data of this work are shown by full circles, the fit to the data with eq. (2) by solid lines. For the explanation of dashed and dotted lines, see caption of fig. 6.

In order to get a better insight into this problem and to compare in more detail with the CELSIUS results, we next consider the angular distributions in dependence of q, defined as half of the relative momentum between the two protons and given by $q^2 = M_{pp}^2/4 - m_p^2$. In this definition q then denotes the momentum of a proton in the pp subsystem. The distribution obtained from our data is compared in fig. 10 with the one given in ref. [9]. Whereas good agreement between both results is found for $q \leq 150\,\mathrm{MeV}/c$, substantial deviations appear for larger-q values. In general large-q values are associated with large opening angles between the protons, which in our experiment are fully covered. However, with the setup at PROMICE/WASA, where protons were detected only for lab angles smaller than 20°, the high-q region was not covered as completely as at TOF and substantial extrapolations had to be applied in the acceptance correction for this part of the CELSIUS data.

4.1 q-dependence of angular distributions

In figs. 11 and 12 we plot pion and proton angular distributions for the four different q regions indicated in fig. 10. The corresponding anisotropy parameters a_2 obtained by fitting eq. (2) to the data are indicated in each of the plots. We see that the pion angular distribution is strongly anisotropic with $a_2 = -1.01(4)$ for the lowest-q range, where there are also results from ref. [9] —and in fact they also exhibit a very strong anisotropy with $a_2 < 0$, though with a large scatter in the data points, see fig. 11. With increasing q the pion angular distributions are get-

ting gradually flatter and for large q the $\Theta_{\pi^0}^{cm}$ distribution gets even curved with $a_2 > 0$.

The lowest-q range ($q < 53\,\mathrm{MeV}/c$) is particularly interesting. It corresponds to a kinetic energy of the protons in the pp subsystem of $T_p^{pp} = q^2/m_p < 3\,\mathrm{MeV}$, a constraint, which has been frequently used to have the pp subsystem safely selected in a relative S-wave state. That way, especially simple configurations in the exit channel are selected allowing a deeper insight into basic reaction mechanisms of π^0 production. In particular, configurations are selected that way, where $pp \to \Delta N(l=1) \to pp\pi^0$, *i.e.*, which have the ΔN system in relative p-wave in the intermediate state. In fact, the observed exceptionally large pion anisotropy of $a_2 = -1.01(4)$ equivalent to a pure $\sin^2\Theta_{\pi^0}^{cm}$ distribution means that at $T_p = 400\,\mathrm{MeV}$ the π^0 production process associated with S-wave protons in the final state happens to be a pure proton spinflip process originating from the transitions ${}^3P_0 \to {}^1S_0 s$ and ${}^3P_2 \to {}^1S_0 d$, where capital letters refer to partial waves in the pp system and small letters to partial waves of π^0 relative to the pp system (see, *e.g.*, table I in ref. [12] for a list of contributing partial waves). In fact, this very special situation has been predicted in the phenomenological model of ref. [8], which —based on the CELSIUS-WASA measurement at $T_p = 310\,\mathrm{MeV}$— gave already a good description of the RCNP data [24] at $T_p = 300$, 318.5, 345 and 390 MeV in the $T_p^{pp} < 3\,\mathrm{MeV}$ range. If we use this model ansatz the cross-section is given by

$$\sigma/\mathrm{PS} \sim \mathrm{FSI}\big[A_0^2 + \big(2A_0B_0\tilde{k}^2 + B_0^2\tilde{k}^4\big)\cos^2\Theta_\pi^{cm}\big] + \tilde{q}^2\big[C^2 + D^2\tilde{k}^2\sin^2\Theta_p^{pp}\big], \quad (3)$$

where PS and FSI stand for phase space and FSI factors (for the latter see eq. (2) of ref. [8]). The pion cm momentum $\tilde{k}$ and the momentum $\tilde{q}$, which is half the relative momentum between the proton pair, are given here in units of the pion mass. A_0 and B_0 denote pion s- and d-wave amplitudes for the transitions ${}^3P_0 \to {}^1S_0 s$ and ${}^3P_2 \to {}^1S_0 d$ —as defined in ref. [8] with $B_0 = -1.2\ A_0$— whereas $C^2 = 0$ and $D = 0.98\ A_0$ stand for proton P-wave contributions of the transitions ${}^1S_0 \to {}^3P_0 s$, ${}^3P_0 \to {}^3P_1 p$ and ${}^3P_1 \to {}^3P_j p$ with $j = 0, 1, 2$, respectively.

If we use eq. (3) together with the parameters A_0, B_0, C^2 and D^2 as determined in ref. [8], then we obtain the dotted curves in figs. 6 and 8-12. The agreement of these calculations with our data is striking for the lowest-q bin (figs. 11, 12) if renormalized to the same absolute cross-section of this bin. Also for the other differential distributions it is partly surprisingly good —with the exception of the proton angular distributions, where the $\sin^2\Theta_p^{pp}$ ansatz badly fails. However, the trend in the pion angular distribution is correctly reproduced. We return to this point in sect. 4.2.

For the pion angular distribution in the lowest-q region a very strong anisotropy with $a_2 < 0$ has recently also been observed in COSY-ANKE measurements at $T_p = 800\,\mathrm{MeV}$ [25]. In a very recent work by Niskanen [26] these anisotropies are explained by a strong energy dependence of the forward cross-section due to interfering pion partial waves.

For the Θ_p^{pp} proton angular distribution, unfortunately, no data are shown in ref. [9] to compare with (there the proton angular distribution in the overall cm system is shown instead, see fig. 9 bottom, which is slightly different from the one in the pp subsystem). In the low-q region, *i.e.* in the region affected most strongly by the pp FSI, we expect the ${}^1S_0$ partial wave between the two protons to dominate. Indeed, we find the Θ_p^{pp} angular distribution to be compatible with isotropy within uncertainties. With increasing q the distribution gets more and more anisotropic with $a_2 < 0$.

The observed trend in the angular distributions is not unexpected. In the low-q region the pp system has kinematically the least internal freedom and hence no chance to develop much dynamics involving higher partial waves. At the same time the pion has kinematically the largest freedom within the $pp\pi^0$ system with the possibility to involve dynamically higher partial waves, which then show up in appreciable anisotropies of the pion angular distributions. At large q the situation is reversed and the pions are kinematically bound to low partial waves, *i.e.* flat angular distributions. The observed anisotropies with negative a_2 values both for proton and pion angular distributions in the lower-q range point to the importance of proton spinflip transitions in this process, which are associated with Δ excitation in the intermediate state as well as with π^0 s- and d-waves in the exit channel. Our results are in support of the conclusions in ref. [8] that π^0 d-waves play an important role already close to threshold, obviously favored by the possibility of exciting the Δ in this manner.

4.2 Improved partial-wave ansatz for the description of data

Finally, we come back to the partial-wave ansatz in ref. [8], which is a simplified version of the more comprehensive ansatz in ref. [9] and which we have seen to work quite well for the pion angular distributions, however, failing badly for the proton distributions. In order to overcome these shortcomings, we modify eq. (3) slightly (and more plausible, if we look at the partial-wave expansions given in refs. [9,12]) by

$$\sigma/\mathrm{PS} \sim \mathrm{FSI}\big[A_0^2 + \big(2A_0B_0\tilde{k}^2 + B_0^2\tilde{k}^4\big)\cos^2\Theta_\pi^{cm}\big] + \tilde{q}^2\big[C^2 + \tilde{k}^2D_1^2\big(1 + D_2(\cos^2\Theta_p^{pp} - 1/3)\big)\big], \quad (4)$$

where the latter coefficients for the Pp waves are related to the one in eq. (3) and in ref. [8] by $D^2 = 2/3D_1^2$ in combination with $D_2 = -3/2$. Note that in this ansatz Ps and Pp contributions are taken into account only very rudimentarily in the hope that still their most important parts are covered by the ansatz. Also for the Sd contribution a $\cos^4\Theta_\pi^{cm}$ term has been neglected due to its smallness and in order to keep the ansatz as close as possible to the one of ref. [8].

Since the model ansatz of ref. [8] works already very well for the pion angular distributions, we do not touch the pion s- and d-wave parts, *i.e.* leave the correlation $B_0 =$

$-1.2\ A_0$, take A_0 as a general scale parameter to reproduce the integral cross-section and adjust C^2, D_1^2, D_2 for best reproduction of the proton angular and q distributions. As a result we obtain

$$B_0 = -1.2\ A_0, \quad C^2 = 0, \quad D_1^2 = 0.22\ A_0^2 \text{ and } D_2 = -0.34.$$

Actually, we get a slightly better description having $C^2 = -0.006$. However, since C^2 as a squared quantity should not be negative, we set $C^2 = 0$ as was done also in ref. [8]. The resulting values mean that aside from Ss and Sd contributions the dominant contribution comes from Pp configurations. The decomposition of the cross-section into interfering Ss and Sd wave contributions is shown in fig. 8 for the M_{pp} invariant-mass distribution. We see that the $Ss + Sd$ wave part adds significantly to the total cross-section and accounts very well for the observed FSI effect in the M_{pp} invariant-mass distribution. Note that Sd contributions, which turn out here to be crucial for the understanding of the negative curvature of the pion angular distributions, have not been taken into account in the analysis of ref. [12].

Though this ansatz is still very simple compared to the full partial-wave ansatz as given in refs. [9,12], it is obviously sufficient to provide a near quantitative description of the data both for angular distributions and invariant masses (dashed lines in figs. 6, 8-12). It is not the aim of this work to provide a perfect partial-wave fit to the data. We rather put here the main emphasis on revealing the dominating partial waves in this reaction, which are responsible for the main signatures in the (unpolarized) differential observables, in particular the angular distributions. Compared to ref. [8] the only major change is the replacement of the D^2 term with its inappropriate $\sin^2\Theta_p^{pp}$-dependence by the D_1^2 and D_2 terms, which provide a more appropriate angular dependence for the protons. This modification, however, is not surprising, since the proton angular dependence has actually not been tested in ref. [8].

From the successful description of our data as well of those treated in ref. [8] we conclude that the ansatz eq. (4) provides an amazingly successful description of the unpolarized $pp \to pp\pi^0$ data from threshold up to $T_p = 400\,\text{MeV}$. However, a word of caution has to be added —in particular concerning the P-wave contributions. As demonstrated in ref. [9] nuclear distortions in the course of the reaction process may change significantly the effective momentum dependence of the partial waves affecting most sensitively the decomposition of different P-wave components. The simple ansatz eq. (4) is rather used here to demonstrate the internal consistency of the experimental differential distributions as well as the importance of d-waves in this reaction. A careful theoretical analysis, which is beyond the scope of this paper, is certainly called for.

5 Summary

It has been demonstrated that by addition of the central calorimeter the COSY-TOF setup is capable of providing a reliable particle identification on the basis of the ΔE-E technique. In this way the different single pion production channels were separated. The results for the $d\pi^+$ channel agree well with previous results. For the $pp\pi^0$ channel significant deviations from previous investigations were obtained for angular distributions as well as for invariant mass spectra. It has been demonstrated, that pions and protons exhibit q-dependent angular distributions. Hence, a full coverage of the phase space appears to be mandatory for reliable experimental results on this issue. For the lower-q region angular distributions with negative a_2 parameter dominate pointing to the importance of proton spinflip transitions associated with π^0 s- and d-waves. In particular, we observe a pure $\sin^2\Theta$ distribution for $T_p^{pp} < 3\,\text{MeV}$, which derives from a special combination of the spinflip transitions ${}^3P_0 \to {}^1S_0 s$ and ${}^3P_2 \to {}^1S_0 d$. Different from previous experiments this has been the first measurement at $T_p \approx 400\,\text{MeV}$ covering practically the full reaction phase space. The data thus may serve as a reliable basis for a comprehensive phase shift analysis of this reaction.

This work has been supported by BMBF, DFG (Europ. Graduiertenkolleg 683) and COSY-FFE. We acknowledge valuable discussions with Christoph Hanhart, Murat Kaskulov, Alexander Sibirtsev, Pia Thorngren-Engblom and Jozef Złomanczuk.

References

1. H.O. Meyer *et al.*, Nucl. Phys. A **539**, 633 (1992).
2. D. Koltun, A. Reitan, Phys. Rev. **141**, 1413 (1966).
3. G.A. Miller, P.U. Sauer, Phys. Rev. C **44**, R1725 (1991).
4. J.A. Niskanen, Phys. Lett. B **289**, 227 (1992).
5. S. Stanislaus *et al.*, Phys. Rev. C **44**, 2287 (1991).
6. G. Rappenecker *et al.*, Nucl. Phys. A **590**, 763 (1995).
7. A. Bondar *et al.*, Phys. Lett. B **356**, 8 (1995).
8. J. Zlomanczuk *et al.*, Phys. Lett. B **436**, 251 (1998).
9. R. Bilger *et al.*, Nucl. Phys. A **693**, 633 (2001).
10. M. Betigeri *et al.*, Phys. Rev. C **65**, 064001 (2002).
11. S. Abd El-Samad *et al.*, Eur. Phys. J. A **17**, 595 (2003).
12. H.O. Meyer *et al.*, Phys. Rev. C **63**, 064002 (2001) and references therein.
13. A. Hassan *et al.*, Nucl. Instrum. Methods A **425**, 403 (1999).
14. M. Dahmen *et al.*, Nucl. Instrum. Methods A **348**, 97 (1994).
15. J. Kress, PhD Thesis, University of Tübingen (2003) `http://w210.ub.uni-tuebingen.de/dbt/volltexte/2003/939`.
16. R.A. Arndt *et al.*, Phys. Rev. C **62**, 034005 (2000); SAID data base, see also `http://said.phys.vt.edu`.
17. CERN Computing and Networks Divison, *GEANT - Detector description and Simulation Tool*, CERN Program Library.
18. S. Keleta, licenciate thesis University of Uppsala (2004).
19. P. Thorngren-Engblom *et al.*, contribution to *MESON 2006, Cracow*, submitted to Phys. Rev. C (nucl-ex/0609003).

20. C. Hanhart, J. Haidenbauer, O. Krehl, J. Speth, Phys. Rev. C **61**, 064008 (2000).
21. P. Deepak, J. Haidenbauer, C. Hanhart, Phys. Rev. C **72**, 024004 (2005).
22. C. Hanhart, Phys. Rep. **397**, 155 (2004) and private communication.
23. V. Lensky *et al.*, Eur. Phys. J. A **27**, 37 (2006).
24. Y. Maeda *et al.*, πN Newslett. **13**, 326 (1997); K. Tamura, Y. Maeda, N. Matsuoka, Nucl. Phys. A **663**, 457c (2000).
25. S. Dymov *et al.*, Phys. Lett. B **635**, 270 (2005) nucl-ex/0512035.
26. J.A. Niskanen, nucl-th/0603072.